

Light Water Reactor Sustainability Program

Quantifying micro-galvanic corrosion in stainless steels activated by post-yielding microstructures



September 2020

U.S. Department of Energy
Office of Nuclear Energy

DISCLAIMER

This information was prepared as an account of work sponsored by an agency of the U.S. Government. Neither the U.S. Government nor any agency thereof, nor any of their employees, makes any warranty, expressed or implied, or assumes any legal liability or responsibility for the accuracy, completeness, or usefulness, of any information, apparatus, product, or process disclosed, or represents that its use would not infringe privately owned rights. References herein to any specific commercial product, process, or service by trade name, trade mark, manufacturer, or otherwise, does not necessarily constitute or imply its endorsement, recommendation, or favoring by the U.S. Government or any agency thereof. The views and opinions of authors expressed herein do not necessarily state or reflect those of the U.S. Government or any agency thereof.

Quantifying micro-galvanic corrosion in stainless steels activated by post-yielding microstructures

Xin Chen ⁽¹⁾, *Maxim Gussev* ⁽²⁾, *Gaurav Sant* ⁽¹⁾

¹ *University of California, Los Angeles, CA, USA*

² *Oak Ridge National Laboratory, Oak Ridge, TN, USA*

September 2020

**Prepared for the
U.S. Department of Energy
Office of Nuclear Energy**

EXECUTIVE SUMMARY

Overview: Plastic strain renders nuclear reactor components more susceptible to stress corrosion cracking (SCC) and premature failure. In this study, for the first time, the strain activation of micro-galvanic corrosion in stainless steels was identified as a cause for SCC. Corrosion and surface reactivity of progressively elongated steels were analyzed using multimodal and multiscale approaches. As a rule, the post-yielding microstructures, e.g., deformation bands and α' -martensites are of lower Volta potentials as compared to the austenite, hence they induce localized corrosion potential gradient, and therefore subjected to accelerated galvanic corrosion. In addition, the dislocation concentrated areas are more reactive, likely due to the reduction in corrosion activation energy resulted from the stored energy. The superposition of surface reactivity and strain distribution revealed that, SCC crack initiation is likely to allocate at the strain concentrated areas wherein micro-galvanic corrosion is favored. The outcomes of this study enhance the mechanistic understanding of how the SCC initiation and propagation are promoted by the pre-existing and crack-induced plastic strain. The innovative approach established in this work can avail the investigation of the irradiation-assisted SCC (IASCC) processes and failure analysis of reactor components.

Implications: The outcomes of this study addresses, N.B., from an electrochemical perspective, the fast oxidation rate observed in the deformation bands, α' -martensite, and dislocation networked areas in reactor environments. In addition, our results imply that, the micro-galvanic corrosion also avails the plastic zone oxidation of a propagating SCC crack. Therefore, this work provides unprecedented insights and critical inputs in developing mechanistic models to predict SCC events in reactor components. More importantly, the methodology developed herein not only is suitable for examining corrosion behavior of “cold-worked” alloys, it can also be applied to unravel the irradiation-induced or irradiation-deformation-activated corrosion mechanisms at micro-to-macro scales. The approaches we developed offer quantitative information on the deformed and corroded alloys, therefore providing possible failure analysis means to enhance the current understanding on the degradation of nuclear reactor components.

ACKNOWLEDGEMENTS

The authors acknowledge financial support for this research from the U.S. Department of Energy's Light Water Reactor Sustainability (LWRS) Program through the Oak Ridge National Laboratory operated by UT-Battelle LLC (Contract #: 4000154999). The contents of this paper reflect the views and opinions of the authors who are responsible for the accuracy of data presented. This research was carried out in the Laboratory for the Chemistry of Construction Materials (LC²) and the California Nanosystems Institute at UCLA. As such, the authors gratefully acknowledge the support that has made these facilities and their operations possible.

CONTENTS

EXECUTIVE SUMMARY	ii
ACKNOWLEDGEMENTS	iii
FIGURE CAPTIONS	v
TABLE CAPTION.....	vii
1. Introduction.....	1
2. Experimental.....	2
3. Results and discussion	4
3.1 Post-yielding microstructural analysis	4
3.2 Determining strain-activated bulk corrosion susceptibility.	6
3.3 Assessing the impact of micro-galvanic corrosion.....	8
4. Conclusions	12
5. References	13

FIGURE CAPTIONS

- Figure 1.** (a) A schematic shows the geometry of the miniature tensile sample used in this work, the dimensions are in mm. (b) The optical photo of the progressively deformed samples. 2
- Figure 2.** The strain-induced microstructure evolution was analyzed by EBSD. (a) Image quality (IQ) maps show the buildup of microstructural defects resulted from the bulk deformation. The localized strain is revealed by the kernel average misorientation (KAM) maps shown in (b), and the development of strain-induced α' -martensite is shown in (c)..... 4
- Figure 3.** Quantification of post-yielding microstructures as functions of the bulk strain: (a) the densities of geometrically necessary dislocations and (b) the α' -martensite contents as measured using the EBSD and a magnetic phase detector. The δ -ferrite contents were measured prior to deformation, and were subtracted in both measurements. The solid line represents the theoretical martensite content calculated based on the Olson-Cohen model²⁵. 5
- Figure 4.** Quantification of strain-induced bulk corrosion behaviors of the 304L stainless steel: (a) reduction in equilibrium potential (b) enhanced corrosion rates and (c) deteriorated passive layer resistances. The experiments are conducted in the deaerated borate buffer solution with lithium chloride, 0.0375 M $\text{Li}_2\text{B}_4\text{O}_7$ + 0.15 M H_3BO_3 + 0.1 M LiCl (pH 8.4). 6
- Figure 5.** The change in steel's surface reactivity is also sensitive to the amount of strain. (a) Tafel plots show a clear dependence of k_{eff} with the amount of strain. (b) Consistently, the calculated k_0 is linearly proportional to the strain. These SECM tests were conducted using the approaching mode in a solution of 0.1 M LiCl+ 2 mM $\text{Ru}(\text{NH}_3)_6\text{Cl}_3$ (pH 5.8)..... 7
- Figure 6.** Apart from the lattice defects, the strain-induced phases also play critical roles in promoting localized corrosion. (a) and (b) are AFM-topography maps shown the strain-induced α' -martensite and deformation bands, which are also of lower surface potentials (i.e., Volta potentials) as compared to the austenite as shown in the SKPFM maps ((c) and (d)). This localized potential gradient give rise to micro-galvanic corrosion, as shown in (e) and (f), the surface reactivities of strain-induced phases are evidently higher. The SECM tests were conducted using the constant-distance mode in a solution of 0.2 M LiCl+ 2 mM $\text{Ru}(\text{NH}_3)_6\text{Cl}_3$ (pH 5.8). 9
- Figure 7.** The strain localization can lead to localized corrosion. For example, a good correlation was identified between the (a) KAM map, and (b) SECM surface reactivity map of the 10% deformed tensile specimen. (c) shows the probability distribution of the normalized current from (left) all mapped areas, and (right) the strain-induced phases represented by the low image quality areas. The SECM tests were conducted using the constant-distance mode in a solution of 0.2 M LiCl+ 2 mM $\text{Ru}(\text{NH}_3)_6\text{Cl}_3$ (pH 5.8).....10
- Figure 8.** The plastic strain activated bulk corrosion sensitivity can be assessed by using the SECM. (a) The COMSOL® simulated von Mises stress and (b) the effective strain distributions of the plastically deformed tensile specimen. (c) Simulated strain distributions along the arrow shown in the inset, and (d) regressed surface reactivity from the same locations shown a consistent

distribution with the plastic strain. The SECM tests were conducted using
approaching mode in a solution of 0.2 M LiCl+ 2 mM Ru(NH₃)₆Cl₃ (pH 5.8).....11

TABLE CAPTION

Table 1. The chemical composition of the 304L stainless steel used (mass %). 2

Quantifying micro-galvanic corrosion in stainless steels activated by post-yielding microstructures

1. Introduction

Mitigating and forecasting stress corrosion cracking (SCC) in reactor components have always been the primary challenge for safely managing the aged nuclear power plants. In any SCC events, inherent crack corrosion is facilitated by the imposition of mechanical load, rendering possible catastrophic failure of the reactor components^{1,2}. Plastic (i.e., post-yielding) deformation, whether was pre-induced^{3,4} or developed in-service⁵, has been identified to play an assisting role in the initiation and propagation of SCC cracks⁶. The impact of deformation on corrosion is significant, so much as in a propagating crack, a plastic zone can be developed at the crack tip, exhibiting an oxidation rate three orders of magnitude higher than the surface⁷. This observed corrosion enhancement has been attributed to the faster diffusion of atoms facilitated by the strain-induced lattice defects^{7,8}. Although such theories offer creditable explanation from a mass-transfer perspective, they discount the chemical/electrochemical potential changes arose from permanently deformed microstructures. The chemical/electrochemical potential mismatch can acutely impact on the alloys' degradation behaviors, for instance, it often leads to localized micro-galvanic corrosion.

To date, micro-galvanic corrosion has only been observed in multi-phase alloys such as magnesium^{9,10} and aluminum alloys^{11,12}, which consist of phases with distinguished compositions. The partitioning of alloy elements renders different surface potentials (i.e., Volta potential) between the constituent phases¹³. Consequently, micro-galvanic couples develop at the phase boundaries, thereby resulting in preferential corrosion of the anodic phase (i.e., vis-à-vis the cathodic phase)¹⁴. However, due to the strain-induced microstructural transformations are diffusion-less, and results in no composition change in stainless steels, the micro-galvanic effects have not been accounted for in the prevailing SCC studies, and therefore excluded from conventional SCC-prediction models¹⁵⁻¹⁷. But it is recently noticed that, post-yielding deformation indeed can alter the Volta potentials of ferrite and austenite phases in a duplex stainless steel, and subsequently inverted galvanic order of the phases and their corrosion rates¹⁸. Thus, plastic deformation can play a critical role inducing galvanic corrosion and promoting SCC. Although important, these impacts have not been addressed for austenitic steels used in nuclear reactors (e.g., 304L and 316L stainless steels).

When plastically deformed, austenitic steels accommodate the bulk strain via the formation of dislocations and lattice transformations. However, strain localization readily occurs at micro-to-macro scales, and likely so is the allocation of corrosion activities. It therefore requires spatially resolved electrochemical characterization methods to unravel the localized corrosion susceptibility. To this end, the scanning Kelvin probe force microscopy (SKPFM) and the scanning electrochemical microscopy (SECM) were employed herein to determine steel's surface reactivity in both the ambient and aqueous environments. By coupling the SKPFM and SECM results with electron backscatter

diffraction (EBSD) analyses, we seek to quantify the micro-galvanic corrosions in stainless steels stimulated by strain-induced lattice transformations, and to offer critical inputs into the developing mechanistic models that forecast the SCC susceptibility of reactor components.

2. Experimental

Sample preparation: A hot rolled 304L stainless steel (ArcelorMittal) with the nominal composition listed in **Table 1** was sectioned into miniature tensile specimens shown in **Figure 1**. The specimens were elongated to 5%, 10%, 22%, and 30% strain under uniaxial tension at a strain rate of 5×10^{-4} /s. To make electrodes, the gauge parts of each sample were sectioned using a low speed diamond wafering saw and attached to a lead wire. The assemblies were then embedded in epoxy resin, and the exposed surfaces were successively polished (N.B., with using the 50 nm colloidal silica as the final step) until the surface featured a mean-roughness $S_a < 10$ nm.

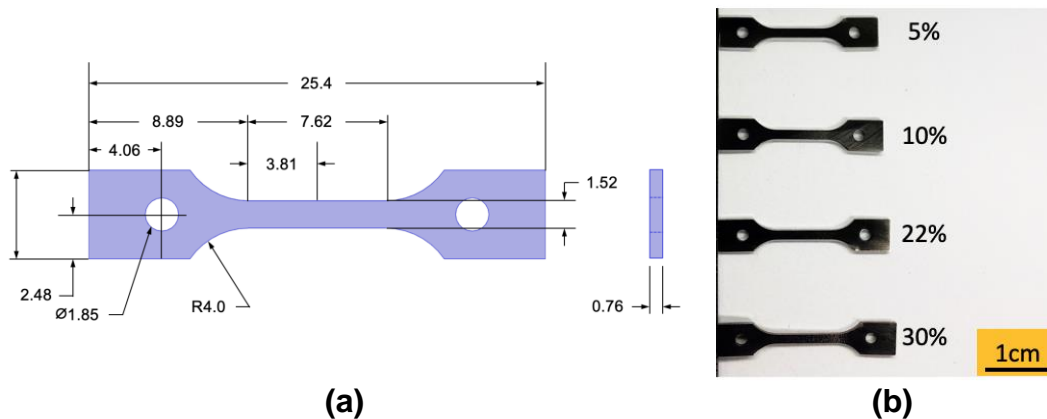


Figure 1. (a) A schematic shows the geometry of the miniature tensile sample used in this work, the dimensions are in mm. (b) The optical photo of the progressively deformed samples.

Table 1. The chemical composition of the 304L stainless steel used (mass %).

Fe	Cr	Ni	Mo	Mn	N	C	Si
bal.	18.29	8.02	0.07	1.28	0.05	0.02	0.45

Microstructure characterization: The crystallographic orientations of the grains were determined using a Scanning Electron Microscopy (SEM, Tescan Mira3) equipped with an EBSD detector (Oxford Ultim Max). The acceleration voltage and step size used were 20 kV and 500 nm, respectively. The EBSD data were subsequently analyzed using the OIM Analysis[®] software. A magnetic phase detector (Fisher technology FMP30) was used to detect the ferrite and martensite contents of the steel specimens prior and post to deformation.

Evaluation of the bulk corrosion behavior: A potentiostat (Princeton Applied Research VersaSTAT 4) equipped with a 20-mL microcell was used to perform bulk

electrochemical experiments. The deformed steels were connected as the working electrode in a system with a platinum wire counter electrode and a Ag/AgCl reference electrode. Bulk electrochemical tests were conducted in a lithium borate buffer solution (Li-BBS, 0.0375M $\text{Li}_2\text{B}_4\text{O}_7$ + 0.15M H_3BO_3) with additional 0.1 M Lithium chloride (LiCl), pH 8.4. The Li-BBS is typically used to simulate the coolant chemistry of light water reactors (LWR)^{7,19,20}, the applied solution is more concentrated in both Li and B in order to provided enough electric conductivity for room-temperature measurements. In addition, LiCl, as a potential coolant contaminate, was added to the solution to accelerate the corrosion tests.

The solution was deaerated by bubbling argon for 1 h prior to each experiment, the solution was unstirred during tests, but the blanket part of the cell was flushed with argon. Potentiostatic (PS) tests were initiated by cathodic cleaning of the working electrode at $-1 V_{\text{Ag}/\text{AgCl}}$ for five minutes, and then the electrodes are equilibrated at open circuit for an hour, and then potentiostatically held at $0.1 V_{\text{Ag}/\text{AgCl}}$ for 2 h. Potentiostatic electrochemical impedance spectroscopy (EIS) was conducted at the same potential after the PS hold. The acquired EIS results were validated using a Kramers-Kronig method²¹ and then analyzed by equivalent circuit modeling using the software ZsimpWin[®] (ver. 3.60).

Surface reactivity analysis: The surface reactivity of the deformed 304L steels were evaluated using a SECM (HEKA EIProScan) operated in feedback mode. The SECM is equipped with a 10 μm Pt ultramicroelectrode (UME) with the RG ratio, i.e., the ratio of the glass-sheath-radius to the Pt-UME-radius, close to 3. The SECM tests were performed with samples immersed in 0.1 and 0.2 M LiCl solutions (pH 5.8) with 2 mM hexaammineruthenium chloride ($\text{Ru}(\text{NH}_3)_6\text{Cl}_3$) as the redox mediator. (N.B., the Li-BBS was not used in SECM measurements to avoid potential complexations between the borate ions and the redox mediator.) A $-0.35 V_{\text{Ag}/\text{AgCl}}$ potential was applied to the UME to promote the diffusion-limiting current of the redox mediator reduction. The surface reactivity was measured using the SECM operated under approaching and constant-distance modes. The former was performed by holding slowly approaching the Pt UME (1 $\mu\text{m}/\text{s}$) to the sample surface while acquiring the current evolution; the latter was performed by tapping the UME to the surface and then lift to a constant distance ($\sim 5 \mu\text{m}$) and scanning the surface point-to-point.

Surface topography and potential analysis: The topography of as polished samples was measured using an atomic force spectroscopy (AFM, Bruker Dimension Icon) operated under the tapping mode. The amplitude-modulated Kelvin probe force spectroscopy (AM-KPFM) was performed using an antimony-doped silicon oxide tip (Bruker PFQNE-AL) with a calibrated work function of 4.09 eV²².

All experiments were performed at the room temperature ($23 \pm 2^\circ\text{C}$). All chemicals used in this study are ACS reagent grade. Solutions were prepared with deionized (DI) water ($>18 \text{ M}\Omega\cdot\text{cm}$).

3. Results and discussion

3.1 Post-yielding microstructural analysis

The steel's microstructure evolution is the prerequisite governing the development of corrosion activities, and it was therefore characterized as the first step. As functions of the bulk strain, lattice defects, encompassing dislocations and strain-induced phases were revealed by the EBSD analyses as shown in **Figure 2**.

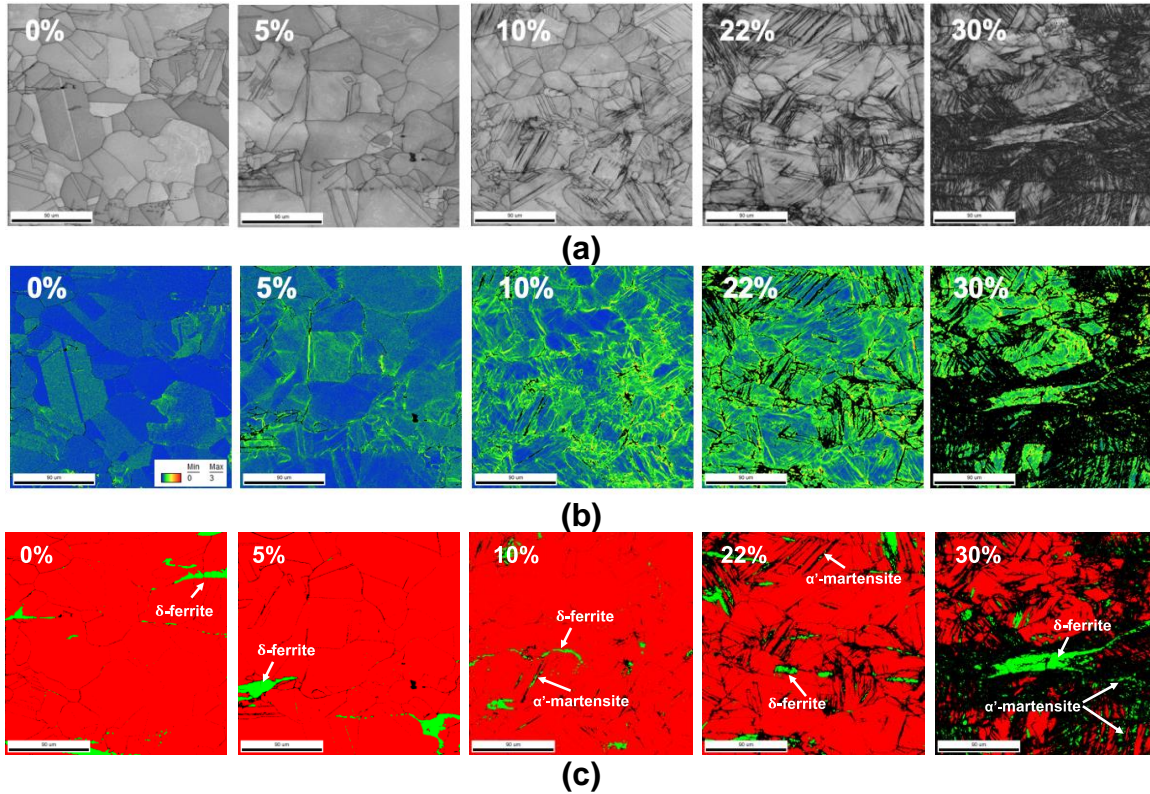


Figure 2. The strain-induced microstructure evolution was analyzed by EBSD. **(a)** Image quality (IQ) maps show the buildup of microstructural defects resulted from the bulk deformation. The localized strain is revealed by the kernel average misorientation (KAM) maps shown in **(b)**, and the development of strain-induced α' -martensite is shown in **(c)**.

As the most common strain-induced defect, dislocations create elastic fields in the surrounding lattice and retain mechanical energy (i.e., the stored energy), and so elevates the chemical energy of steel atoms²³. Therefore, the dislocation density is closely related to the corrosion reactivity. In specific, the accumulation of geometrically necessary dislocations (GND) drives grain rotation during tensile testing, and the GND density can be revealed by the kernel average misorientation (KAM) analysis²⁴: $\rho_{GND} = \frac{2\vartheta}{b\mu}$ [Eq. 1], where ϑ is the KAM angle, b is the magnitude of burger's vector, and μ is the EBSD step size (500 nm). As seen from **Figure 2b**, the distribution of dislocations is not uniform at the microscale. The KAM maps highlight the localized variation in GND densities, for instance, regions adjacent to grain and phase boundaries are often of high

KAM angles, indicating higher dislocation concentration, and, therefore, stored energy in these regions. Stemmed from the localized accumulation of dislocations, the averaged GND densities also increase proportionally as a function of the bulk strain (see **Figure 3a**). Note that, the GND density was calculated using the area-averaged KAM values.

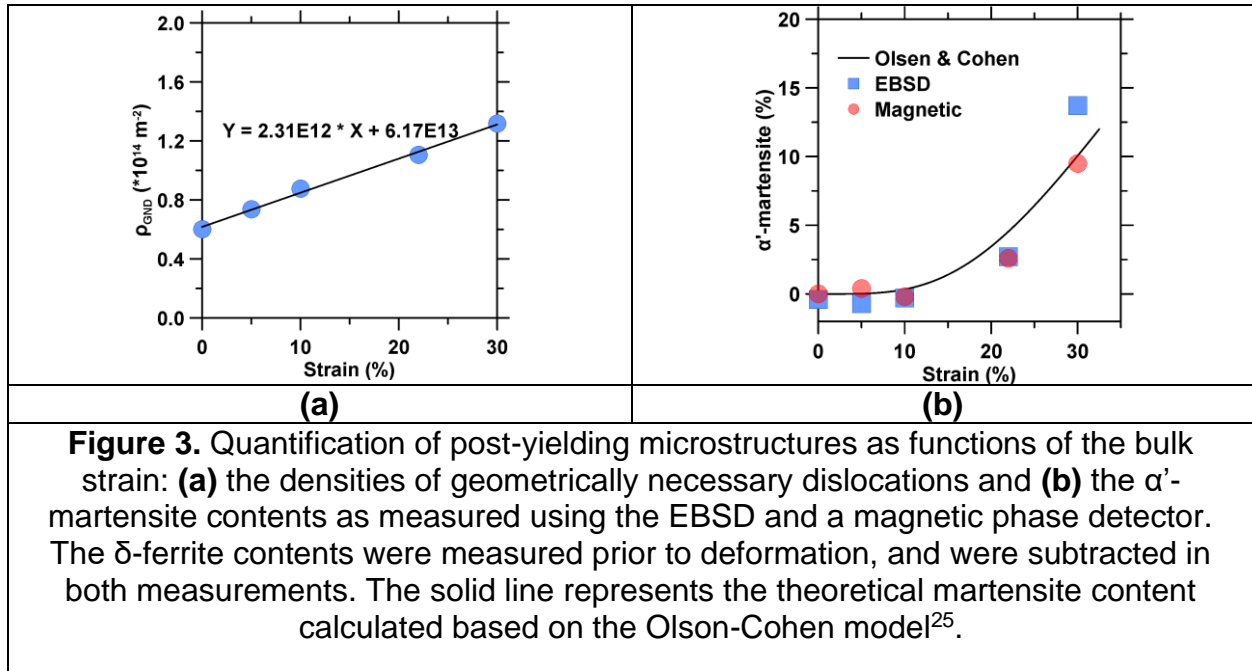


Figure 3. Quantification of post-yielding microstructures as functions of the bulk strain: **(a)** the densities of geometrically necessary dislocations and **(b)** the α' -martensite contents as measured using the EBSD and a magnetic phase detector. The δ -ferrite contents were measured prior to deformation, and were subtracted in both measurements. The solid line represents the theoretical martensite content calculated based on the Olson-Cohen model²⁵.

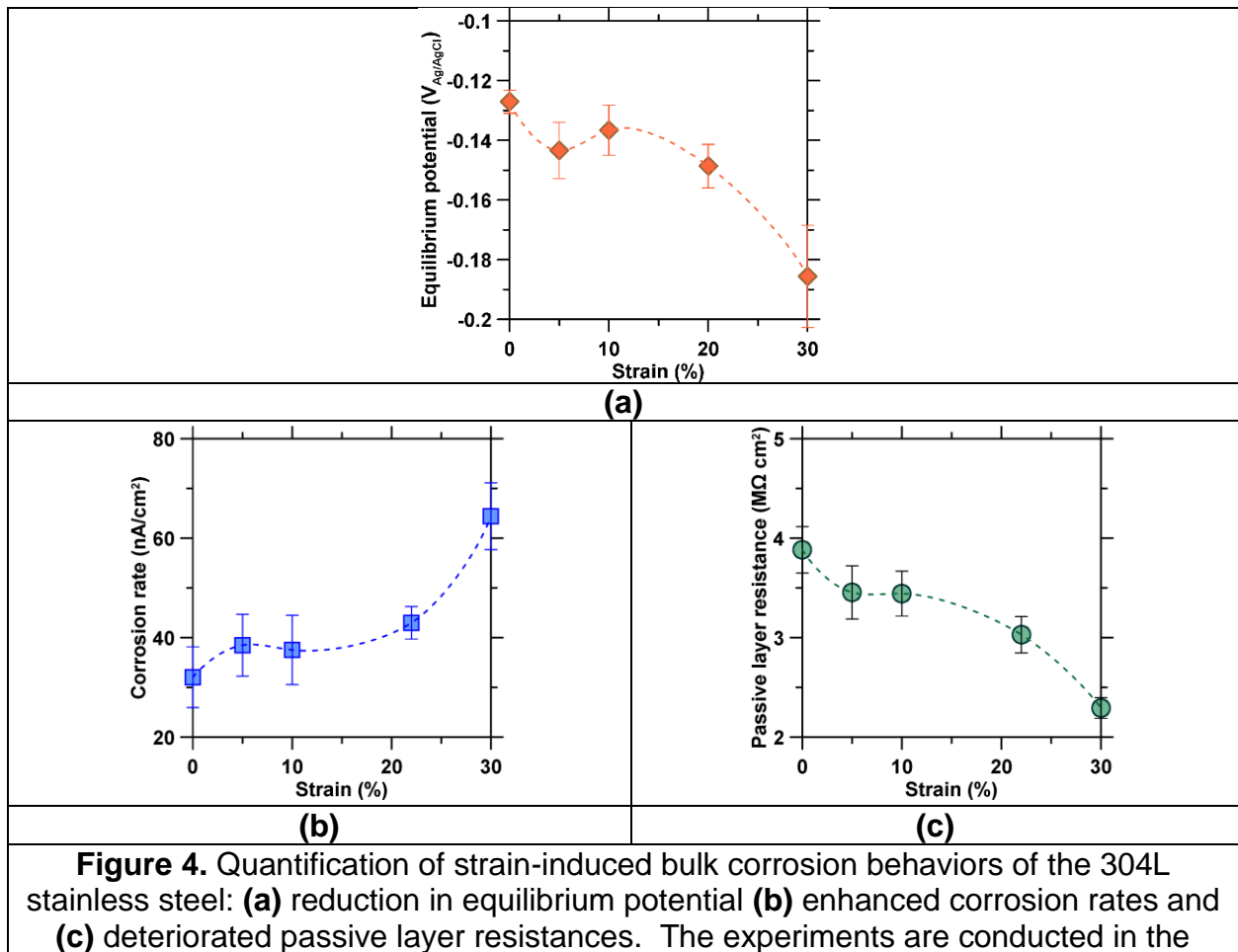
On the other hand, dislocation development can only result in a limiting localized misorientation angle of $< 2^\circ$, further microstructural heterogeneity is attributed to the strain-induced phase transformations. Among the strain-induced phases, the large α' -martensite domains has a body-centered-cubic (bcc) structure and a lath-like morphology, thereby can be revealed by the phase map shown in **Figure 2c**. Based on the volumetric analyses (as shown in **Figure 3b**), detectable amounts of strain-induced α' -martensite emerged in the 10% deformed sample and grew in volume as the strain increases. In addition, a large fraction of small martensite domains and deformation bands render poor electron diffraction patterns, they are denoted as dark areas in the image quality (IQ) as well as the other EBSD maps. By comparing the KAM and phase distribution images, one can notice that the deformation bands and martensites preferentially develops at dislocation concentrated areas, suggesting the dislocation accumulation stimulates the strain-induced phase transformations. Such the assertion can also be confirmed by the observation that, strain-induced phases are generally allocated adjacent to δ -ferrite inclusions, which can impede dislocation motion and cause dislocation accumulation²⁶.

Unlike dislocation formation processes, strain-induced phase transformations are usually exothermic²⁷, implying the resulted phases do not directly contribute to the stored energy²⁸. However, due to the microstructurally defective nature of deformation

bands and the α' -martensite, their roles in inducing localized corrosion were subsequently assessed.

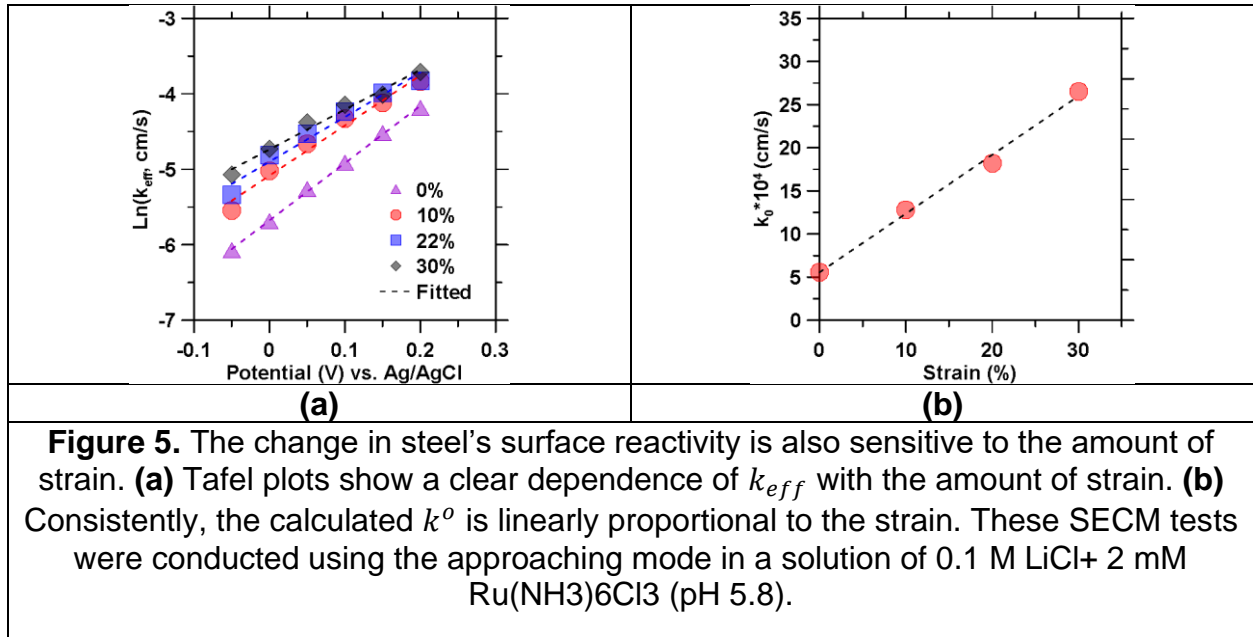
3.2 Determining strain-activated bulk corrosion susceptibility.

In order to correlate the steel's post-yielding microstructure with corrosion reactivity, the progressively deformed samples were characterized via electrochemical means. A detreated borate buffer solution was used representing a chlorine-contaminated reactor coolant composition. In this solution, equilibrium potentials (i.e., corrosion potentials) were measured following a one-hour immersion. As a result, evident reduction in corrosion potentials were observed as the bulk deformation increases (**Figure 4a**): for instance, the corrosion potential of the 30 % deformed 304L is about 60 mV lower than the undeformed control. This indicates that, strain-induced microstructures clearly lead to bulk corrosion instability of the 304L. More importantly, the corrosion potentials are decisive of the galvanic series of alloys²⁹, the greatly deformed samples are therefore less noble than samples with smaller amounts of strain.

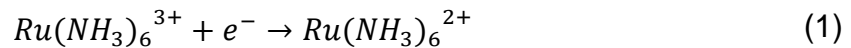


deaerated borate buffer solution with lithium chloride, 0.0375 M $\text{Li}_2\text{B}_4\text{O}_7$ + 0.15 M H_3BO_3 + 0.1 M LiCl (pH 8.4).

Such insights are also supported by the anodic behaviors of deformed 304L in the same solution. An anodic potential of 0.1 $V_{\text{Ag}/\text{AgCl}}$ was applied to simulate an oxidizing reactor environment resulted from reactor coolant radiolysis^{30–32}. When polarized, the 304L steel passives and its corrosion current attains a steady-state rate after a two-hour potentiostatic hold. The steady-state corrosion rate (as shown in **Figure 4b and 4c**,) doubled from 32 nA/cm² to 64 nA/cm² as the deformation increased from 0 to 30 %, whereas the passive layer resistance reduced from 3.9 M Ω cm² to 2.3 M Ω cm², also by a factor of ~2. As evidenced, the formation of less resistant passive layers can also be attributed to the post-yielding microstructures. This is significant since, in reactor environments, the passive layer impedes the steel's redox interactions with the strong oxidant produced by coolant radiolysis (e.g. hydroxyl radicals and H_2O_2)³³, and defective passive layers enhance steel's in-reactor reactivity.



As such, SECM was employed to characterize the surface reactivity availed by post-yielding microstructures. By adding a trace-amount of redox mediator (2mM $\text{Ru}(\text{NH}_3)_6\text{Cl}_3$) in solution, the SECM measures the reduction current of the following reaction:



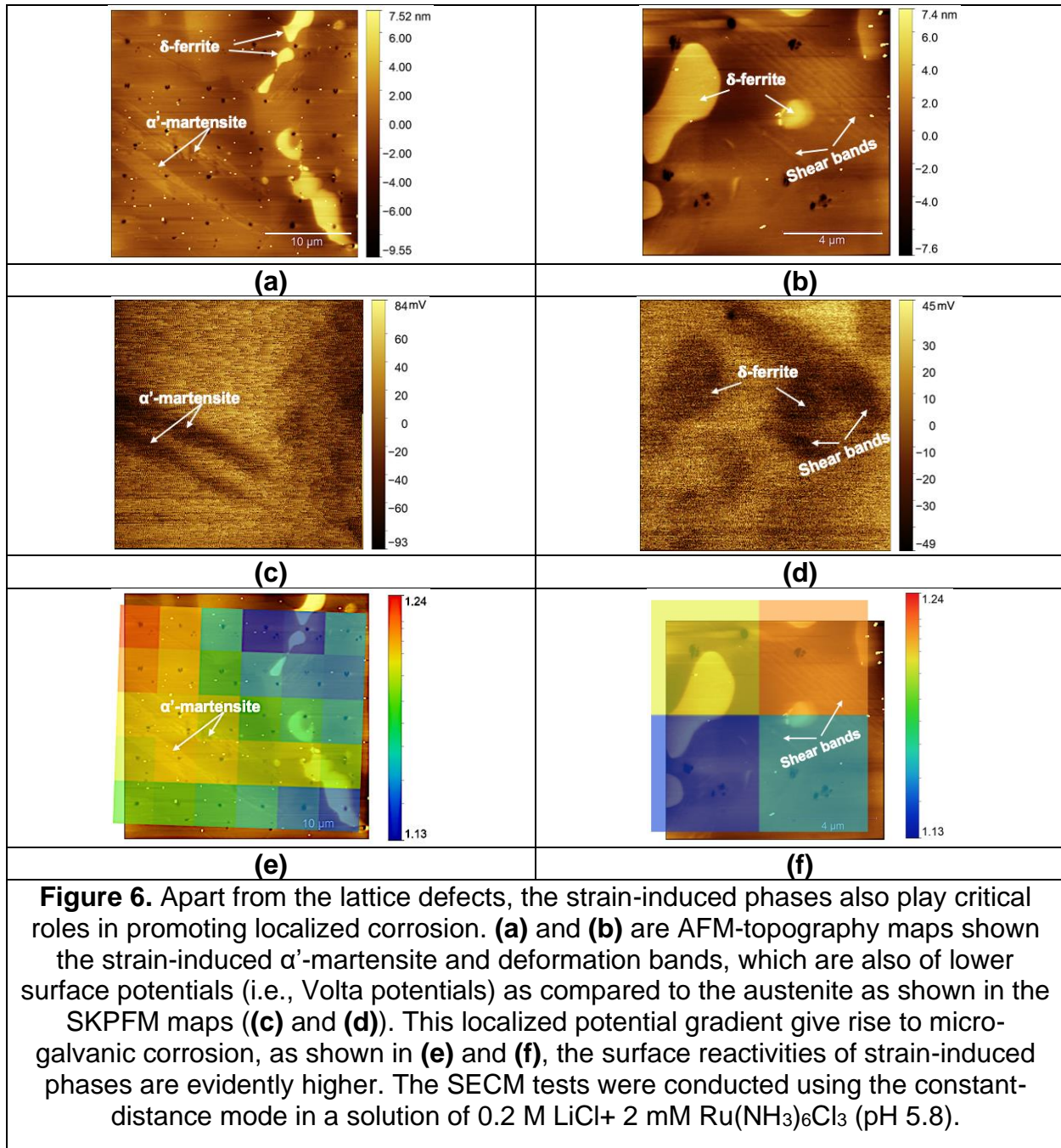
A diffusion-limiting reduction current, i_0 , was attained when the SECM probe (i.e., the Pt ultramicroelectrode, UME) was far away from the steel surface. By approaching the Pt UME towards the steel surface, the UME-reduced $\text{Ru}(\text{NH}_3)_6^{2+}$ was oxidized by the steel surface to form $\text{Ru}(\text{NH}_3)_6^{3+}$ (through the reverse process of **Reaction 1**). Then the SECM probe acquired the feedback from surface-generated $\text{Ru}(\text{NH}_3)_6^{3+}$, and measured

an integrated current I_{UME} . The reactivity of steel's passive film is characterized by the generation rate constant of $Ru(NH_3)_6^{3+}$, k_{eff} (in cm/s), which can be quantified by analyzing the approach curve of the normalized UME currents (I_{UME} / I_0).

As shown in the Tafel plots (**Figure 5a**), at a fixed amount of strain, the k_{eff} dependence with the applied potentials are well-governed by the Butler-Volmer relationship³⁴: $k_{eff} = k^0 \exp[\frac{\alpha n F}{RT} (E - E^{0'})]$ [**Eq. 2**], where k^0 is the standard rate constant, α is the charge transfer coefficient, n is the number of electrons, F is the Faraday constant, R is the gas constant, T is the temperature, E is the applied potential, and $E^{0'}$ is the standard potential of the $Ru(NH_3)_6^{3+/2+}$ redox couple. As depicted in **Figure 5b**, the regressed k^0 coincide with k_{eff} , both of which were elevated by the post-yielding strain, indicating that post-yielding microstructures renders more reactive surface. In fact, the observations are consistent with the measured surface reactivity of the 304L when subjected to only elastic stresses^{35,36}. And similar surface reactivity enhancement has also been observed for the Ni-based austenitic alloys under both compressive and tensile stresses³⁷. Taken together, the post-yielding microstructures activate the surface reactivity in a similar way as the elastic stresses, i.e., by inducing defects in passive films and to synergize charge transfer reactions at the film/solution interface. Consequently, the surface reactivity of the 304L steel is governed by the amount of deformation, yielding a linear dependence of k^0 on the strain.

3.3 Assessing the impact of micro-galvanic corrosion

As the localization of post-yielding microstructures is evident based on EBSD analyses (**Figure 2**), the steel surface may not exhibit uniform corrosion activities. For instance, due to the increasing strain resulted in reduction of bulk corrosion potentials (**Figure 4a**), the localized potential gradient – a key element to induct micro-galvanic corrosion – is likely to rise owing to the strain localization. Thus, the surface potential distribution in a 10% deformed 304L was assessed using SKPFM. The results (see **Figure 6a-d**) reveal that, the strain-induced α' -martensite, and shear bands exhibit surface potentials (i.e., Volta potentials) about 60 mV lower as compared to the austenitic matrices. Such the potential difference is consistent with the corrosion potential reduction measured in solution (**Figure 4a**), implying the reduction in bulk corrosion potential was stemmed from the development of α' -martensite and deformation bands. (N.B., based on our results, the SKPFM is not able to detect any surface potential variation related to dislocation concentrations.) The lower Volta potential corresponds to the lower energy cost to extract electrons via charge transfer reactions^{38,39}, and an excellent correlation has been established between the Volta potential and in-solution corrosion potentials⁴⁰. Therefore, the α' -martensite and deformation bands are electrochemically less noble than the austenitic matrix. The micro-galvanic corrosion is expected to take place, wherein the strain-induced phases preferentially corrodes as the anode, whereas the austenite is cathodically protected.



To profile the micro-galvanic corrosion at the steel surface, constant-distance SECM analyses were performed: the Pt UME were halted at 3 μm above the SKPFM-scanned area and measured the redox mediator's reaction current. As depicted in **Figure 6e and 6f**, the higher current is consistently observed at the lower surface potential areas, indicating the strain-induced α' -martensite and shear bands also have higher surface reactivity as compared to the less reactive austenite. These multimodal analyses demonstrated the strain-induced phases are subjected to accelerated corrosion owing to the micro-galvanic coupling.

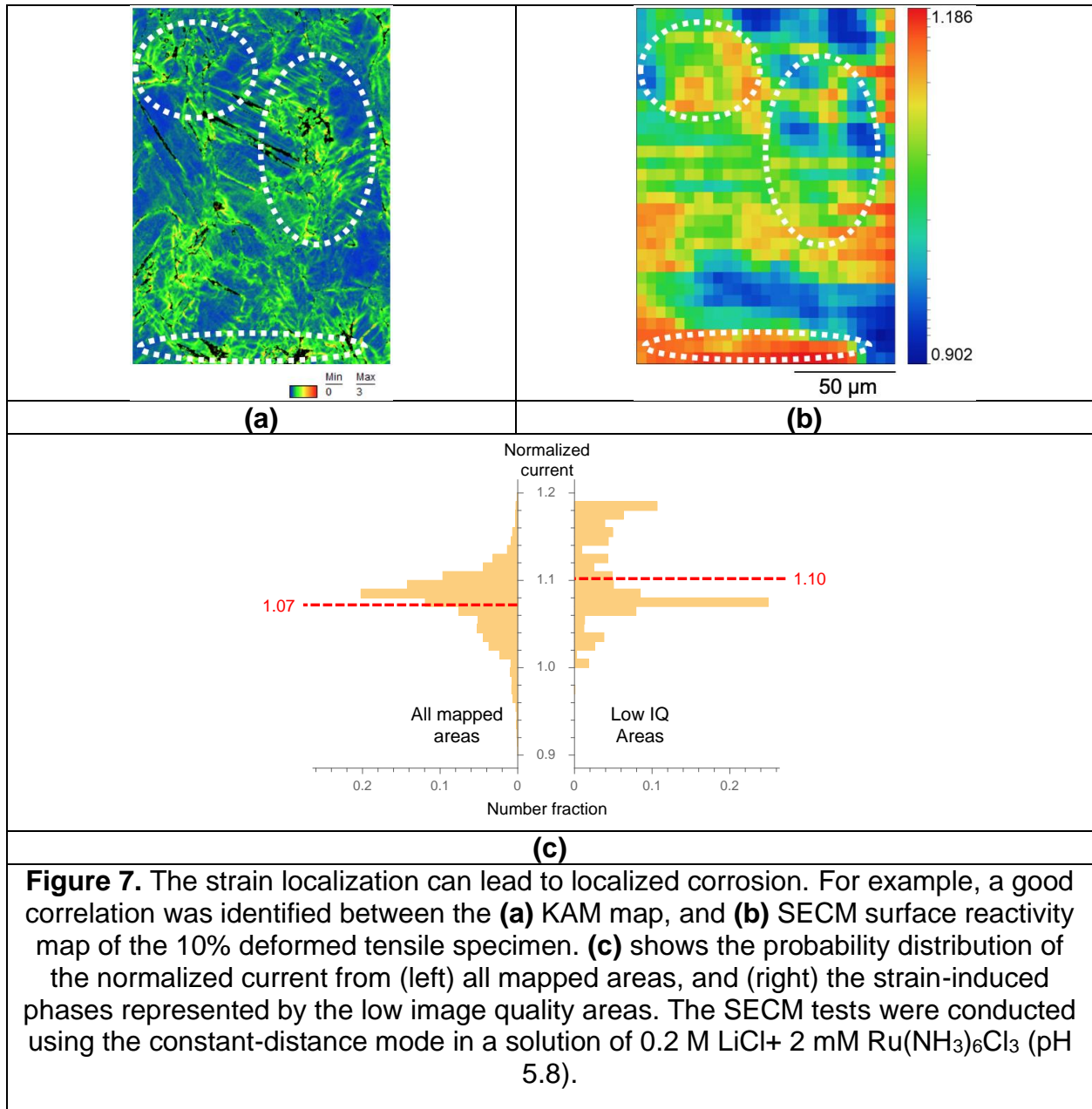
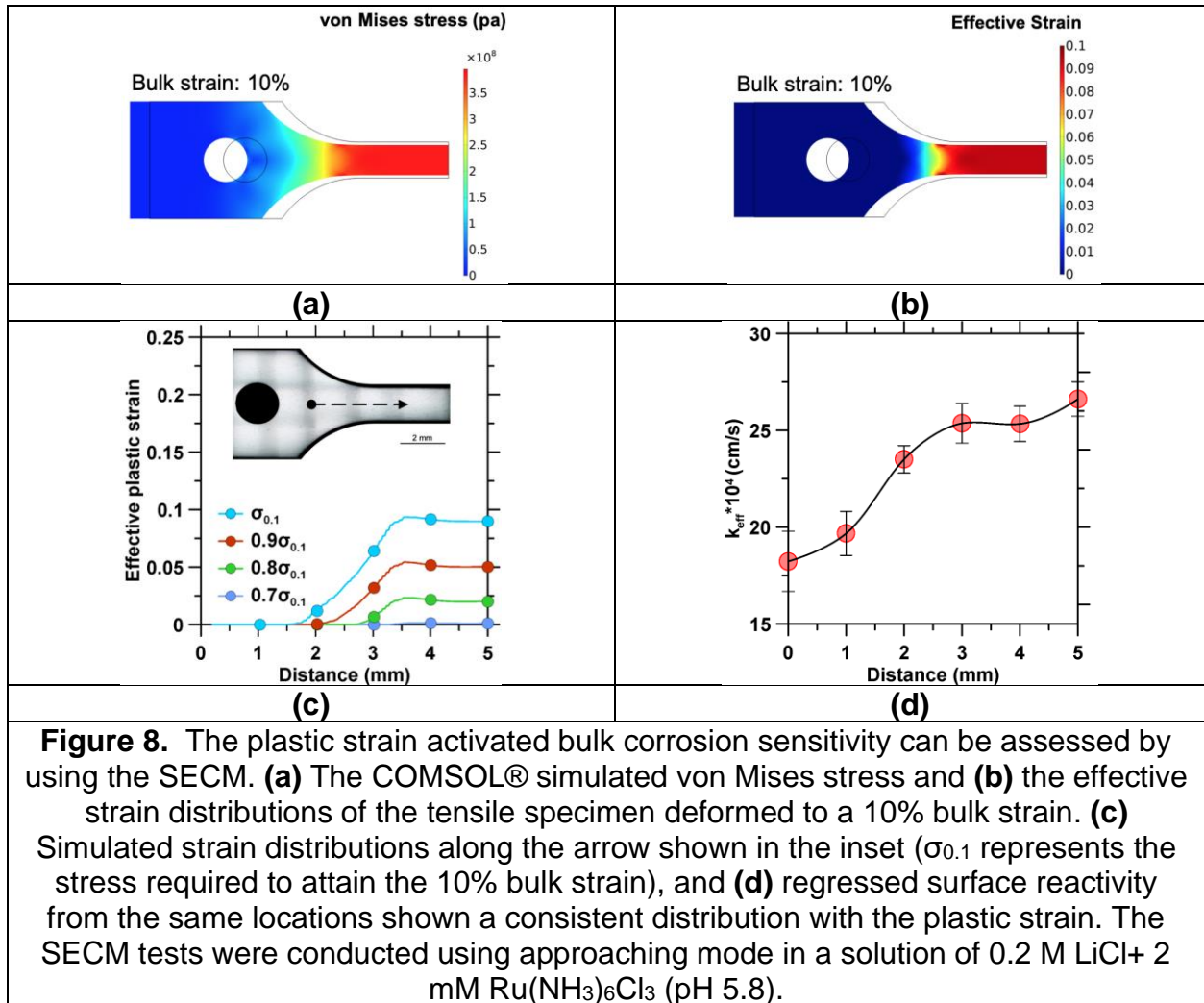


Figure 7. The strain localization can lead to localized corrosion. For example, a good correlation was identified between the **(a)** KAM map, and **(b)** SECM surface reactivity map of the 10% deformed tensile specimen. **(c)** shows the probability distribution of the normalized current from (left) all mapped areas, and (right) the strain-induced phases represented by the low image quality areas. The SECM tests were conducted using the constant-distance mode in a solution of 0.2 M LiCl+ 2 mM Ru(NH₃)₆Cl₃ (pH 5.8).

The EBSD results showed the localization of post-yielding microstructures, the micro-galvanic corrosion activities are likely to follow. As such, the EBSD-KAM and SECM-surface reactivity were mapped and compared from the same area of the steel surface (**Figure 7**). As indicated by the circled regions in **Figure 7a and 7b**, higher surface reactivities are generally associated with higher strain concentrations. In particular, **Figure 7c** shows that the strain-induced phases (represented by the low IQ areas, i.e., the dark regions shown in **Figure 7a**) were disposed to exhibit upper-bound currents, and the average is also higher vis-à-vis all measured areas. Furthermore, the circled regions are also indicative of that, the areas of higher reactivity are generally associated with larger KAM angles. As aforementioned, greater KAM angles denote

higher dislocation concentrations, consequently, higher stored energy is stored in these areas that activates surface reactions and steel corrosion.

On the other hand, because the SECM readily integrated responses from crystallographic features, e.g., grain boundaries and grain orientations⁴¹, the convoluted surface reactivity distribution is not entirely in congruent with the strain localization when measured at grain-level scales. For instance, mismatches between the surface reactivity and KAM maps can be observed in **Figure 7**. To exclude such the crystallographic influences, the impact of micro-galvanic corrosion was evaluated at a macro-scale that encompasses hundreds of diversely oriented grains.



The macro-scale strain is expected to vary in the tensile specimens employed by this work (**Figure 1a**). A COMSOL® simulation was performed to determine the stress-strain distribution in the bulk. The simulation utilized a nonlinear elastoplastic model, wherein the post-yielding stress-strain relation is defined by the Ludwik relationship⁴²: $\sigma_{ys} = \sigma_{ys0} + k(\epsilon_{pe})^n$ [Eq. 3], where σ_{ys} is the stress beyond the yielding point, σ_{ys0} is the yield stress (215 MPa), ϵ_{pe} is the effective plastic strain, and k (1033 Mpa) and n

(0.768) are coefficients fitted from the experimental true-stress-strain curve. Based on the simulated results (**Figure 8a and 8b**), the post-yielding strain distributed uniformly at the gauge part but lessened at regions closed to the sample's head. The line profiles shown in **Figure 8c** depict the progressively increasing and then plateaued effective strain under successively increased stresses.

Due to the effective strain accumulated at the gauge part, it is expected to have concentrated strain-induced microstructures and pronounced corrosion micro-galvanic activities. In fact, as shown in **Figure 8c and 8d**, greater k_{eff} values were exhibited by the gauge part, whereas the tensile head is relatively inert. The distribution of surface reactivity is in congruent with that of the plastic strain. Interestingly, the micro-galvanic coupling resulted in a partitioned macro-corrosion reactivity. This implies that, localized corrosion is favored to initiate in the component with higher amount of deformation, wherein acute micro-galvanic corrosion can lead to the formation of micro-pits and crevices, which can further develop into SCC cracks. As for a propagating SCC crack, the micro-galvanic corrosion also explains why the plastic zone oxides at much faster rates^{7,43}. Through surface reactivity analyses, the SECM provide feasible means to detect or predict the SCC susceptibilities at the micro- and bulk- scales.

4. Conclusions

Taken together, this work determined that, localization of post-yielding microstructures induces the micro-galvanic corrosion in stainless steels. Specifically, the dislocations contribute to the stored energy and elevated the steel's chemical potential and corrosion reactivity. On the other hand, the deformation bands and strain-induced martensites are determined to have lower Volta potentials vis-à-vis the austenitic matrix, rendering surface potential heterogeneity. The localized potential gradients are the prerequisite inducing micro-galvanic corrosion; indeed, we have observed the enhancement in both the localized and the bulk corrosion reactivity. The outcomes of this study addresses, N.B., from an electrochemical perspective, the fast oxidation rate observed in the deformation bands, α' -martensite, and dislocation networked areas in reactor environments^{8,44}. In addition, our results imply that, the micro-galvanic corrosion also avails the plastic zone oxidation of a propagating SCC crack. Therefore, this work provides unprecedented insights and critical inputs in developing mechanistic models to predict SCC events in reactor components. More importantly, the methodology developed herein not only is suitable for examining corrosion behavior of "cold-worked" alloys, it can also be applied to unravel the irradiation-induced or irradiation-deformation-activated corrosion mechanisms at micro-to-macro scales. The approaches we developed offer quantitative information on the deformed and corroded alloys, therefore providing possible failure analysis means to enhance the current understanding on the degradation of nuclear reactor components.

5. References

- (1) Kondo, S. Lessons Learned for PSA from the SGTR Incident at Mihama, Unit 2, in 1991. *Reliability Engineering & System Safety* **1994**, *45* (1–2), 57–65.
- (2) Matsubara, N.; Kobayashi, T.; Fujimoto, K.; Nomura, Y.; Chigusa, N.; Hirano, S. Research Programs on SCC of Cold-Worked Stainless Steel in Japanese PWR NPP. In *International Symposium Fontevraud*; 2011; Vol. 7, p A099.
- (3) Hamilton, M. L.; Huang, F.-H.; Yang, W. J.; Garner, F. A. Mechanical Properties and Fracture Behavior of 20% Cold-Worked 316 Stainless Steel Irradiated to Very High Neutron Exposures. In *Influence of Radiation on Material Properties: 13th International Symposium (Part II)*; ASTM International, 1987.
- (4) Takakura, K.; Nakata, K.; Ando, M.; Fujimoto, K.; Wachi, E. Lifetime Evaluation for IASCC Initiation of Cold Worked 316 Stainless Steel's BFB in PWR Primary Water. In *Proceedings of the 13th International Conference on Environmental Degradation of Materials in Nuclear Power Systems*; 2007.
- (5) Was, G. S. *Fundamentals of Radiation Materials Science: Metals and Alloys*; Springer, 2016.
- (6) Andresen, P. L.; Angeliu, T. M.; Horn, R. M.; Catlin, W. R.; Young, L. M. Effect of Deformation on SCC of Unsensitized Stainless Steel. In *CORROSION 2000*; NACE International, 2000.
- (7) Shen, Z.; Du, D.; Zhang, L.; Lozano-Perez, S. An Insight into PWR Primary Water SCC Mechanisms by Comparing Surface and Crack Oxidation. *Corrosion Science* **2019**, *148*, 213–227.
- (8) Lozano-Perez, S.; Yamada, T.; Terachi, T.; Schröder, M.; English, C. A.; Smith, G. D. W.; Grovenor, C. R. M.; Eyre, B. L. Multi-Scale Characterization of Stress Corrosion Cracking of Cold-Worked Stainless Steels and the Influence of Cr Content. *Acta Materialia* **2009**, *57* (18), 5361–5381.
- (9) Coy, A. E.; Viejo, F.; Skeldon, P.; Thompson, G. E. Susceptibility of Rare-Earth-Magnesium Alloys to Micro-Galvanic Corrosion. *Corrosion Science* **2010**, *52* (12), 3896–3906.
- (10) Cai, C.; Song, R.; Wang, L.; Li, J. Effect of Anodic T Phase on Surface Micro-Galvanic Corrosion of Biodegradable Mg-Zn-Zr-Nd Alloys. *Applied Surface Science* **2018**, *462*, 243–254.
- (11) Schmutz, P.; Frankel, G. S. Characterization of AA2024-T3 by Scanning Kelvin Probe Force Microscopy. *Journal of the Electrochemical Society* **1998**, *145* (7), 2285–2295.
- (12) Zhang, F.; Örneek, C.; Nilsson, J.-O.; Pan, J. Anodisation of Aluminium Alloy AA7075–Influence of Intermetallic Particles on Anodic Oxide Growth. *Corrosion Science* **2020**, *164*, 108319.
- (13) Melitz, W.; Shen, J.; Kummel, A. C.; Lee, S. Kelvin Probe Force Microscopy and Its Application. *Surface science reports* **2011**, *66* (1), 1–27.
- (14) Liu, J.; Song, Y.; Chen, J.; Chen, P.; Shan, D.; Han, E.-H. The Special Role of Anodic Second Phases in the Micro-Galvanic Corrosion of EW75 Mg Alloy. *Electrochimica Acta* **2016**, *189*, 190–195.
- (15) Saito, K.; Kuniya, J. Mechanochemical Model to Predict Stress Corrosion Crack Growth of Stainless Steel in High Temperature Water. *Corrosion Science* **2001**, *43* (9), 1751–1766.

- (16) MacDonald, D. D.; Urquidi-MacDonald, M. A Coupled Environment Model for Stress Corrosion Cracking in Sensitized Type 304 Stainless Steel in LWR Environments. *Corrosion Science* **1991**, *32* (1), 51–81.
- (17) Newman, R. C. Developments in the Slip-Dissolution Model of Stress Corrosion Cracking. *Corrosion* **1994**, *50* (9), 682–686.
- (18) Örnek, C.; Engelberg, D. L. SKPFM Measured Volta Potential Correlated with Strain Localisation in Microstructure to Understand Corrosion Susceptibility of Cold-Rolled Grade 2205 Duplex Stainless Steel. *Corrosion Science* **2015**, *99*, 164–171.
- (19) Chen, Y.; Urquidi-Macdonald, M.; Macdonald, D. D. The Electrochemistry of Zirconium in Aqueous Solutions at Elevated Temperatures and Pressures. *Journal of Nuclear Materials* **2006**, *348* (1–2), 133–147.
- (20) Aaltonen, P.; Hanninen, H. *Water Chemistry and Behavior of Materials in PWRs and BWRs*; 1997.
- (21) Boukamp, B. A. A Linear Kronig-Kramers Transform Test for Immittance Data Validation. *Journal of the electrochemical society* **1995**, *142* (6), 1885–1894.
- (22) Kazakova, O.; Panchal, V.; Burnett, T. L. Epitaxial Graphene and Graphene-Based Devices Studied by Electrical Scanning Probe Microscopy. *Crystals* **2013**, *3* (1), 191–233.
- (23) Bever, M. B.; Holt, D. L.; Titchener, A. L. The Stored Energy of Cold Work. *Progress in materials science* **1973**, *17*, 5–177.
- (24) Calcagnotto, M.; Ponge, D.; Demir, E.; Raabe, D. Orientation Gradients and Geometrically Necessary Dislocations in Ultrafine Grained Dual-Phase Steels Studied by 2D and 3D EBSD. *Materials Science and Engineering: A* **2010**, *527* (10–11), 2738–2746.
- (25) Olson, G. B.; Cohen, M. Kinetics of Strain-Induced Martensitic Nucleation. *Metallurgical transactions A* **1975**, *6* (4), 791.
- (26) Czerwinski, F.; Cho, J. Y.; Brodtko, A.; Zielinska-Lipiec, A.; Sunwoo, J. H.; Szpunar, J. A. The Edge-Cracking of AISI 304 Stainless Steel during Hot-Rolling. *Journal of materials science* **1999**, *34* (19), 4727–4735.
- (27) Cios, G.; Tokarski, T.; Żywczak, A.; Dziurka, R.; Stępień, M.; Marciszko, M.; Pawłowski, B.; Wieczerek, K.; Bała, P. The Investigation of Strain-Induced Martensite Reverse Transformation in AISI 304 Austenitic Stainless Steel. *Metallurgical and Materials Transactions A* **2017**, *48* (10), 4999–5008.
- (28) Shin, H. C.; Ha, T. K.; Chang, Y. W. Kinetics of Deformation Induced Martensitic Transformation in a 304 Stainless Steel. *Scripta Materialia* **2001**, *45* (7), 823–829.
- (29) Hack, H. P. Evaluating Galvanic Corrosion. *Anonymous ASM Handbook* **2003**, *13*, 562–567.
- (30) Was, G. S.; Andresen, P. L. Irradiation-Assisted Stress-Corrosion Cracking in Austenitic Alloys. *JOM* **1992**, *44* (4), 8–13.
- (31) Glass, R. S.; Overturf, G. E.; Van Konynenburg, R. A.; McCright, R. D. Gamma Radiation Effects on Corrosion—I. Electrochemical Mechanisms for the Aqueous Corrosion Processes of Austenitic Stainless Steels Relevant to Nuclear Waste Disposal in Tuff. *Corrosion Science* **1986**, *26* (8), 577–590.
- (32) Chen, X.; Ebert, W. L.; Indacochea, J. E. Electrochemical Corrosion of a Noble Metal-Bearing Alloy-Oxide Composite. *Corrosion Science* **2017**, *124*, 10–24.

- (33) Raiman, S. S.; Bartels, D. M.; Was, G. S. Radiolysis Driven Changes to Oxide Stability during Irradiation-Corrosion of 316L Stainless Steel in High Temperature Water. *Journal of Nuclear Materials* **2017**, *493*, 40–52.
- (34) Bard, A. J.; Faulkner, L. R. *Electrochemical Methods: Fundamentals and Applications*, 2nd ed.; John Wiley & Sons, 2001; Vol. 2.
- (35) Sidane, D.; Devos, O.; Puiggali, M.; Touzet, M.; Tribollet, B.; Vivier, V. Electrochemical Characterization of a Mechanically Stressed Passive Layer. *Electrochemistry Communications* **2011**, *13* (12), 1361–1364.
- (36) Sidane, D.; Touzet, M.; Devos, O.; Puiggali, M.; Larivière, J. P.; Guitard, J. Investigation of the Surface Reactivity on a 304L Tensile Notched Specimen Using Scanning Electrochemical Microscopy. *Corrosion Science* **2014**, *87*, 312–320.
- (37) Zhu, R. K.; Luo, J. L. Investigation of Stress-Enhanced Surface Reactivity on Alloy 800 Using Scanning Electrochemical Microscopy. *Electrochemistry Communications* **2010**, *12* (12), 1752–1755.
- (38) Hurley, M. F.; Efav, C. M.; Davis, P. H.; Croteau, J. R.; Graugnard, E.; Birbilis, N. Volta Potentials Measured by Scanning Kelvin Probe Force Microscopy as Relevant to Corrosion of Magnesium Alloys. *Corrosion* **2014**, *71* (2), 160–170.
- (39) Cheon, J. Y.; Kim, J. H.; Kim, J. H.; Goddeti, K. C.; Park, J. Y.; Joo, S. H. Intrinsic Relationship between Enhanced Oxygen Reduction Reaction Activity and Nanoscale Work Function of Doped Carbons. *Journal of the American Chemical Society* **2014**, *136* (25), 8875–8878.
- (40) Schmutz, P.; Frankel, G. S. Characterization of AA2024-T3 by Scanning Kelvin Probe Force Microscopy. *Journal of the Electrochemical Society* **1998**, *145* (7), 2285–2295.
- (41) Verchère, L.; Aubert, I.; Devos, O. Influence of the Crystallographic Orientation on the Electrochemical Reactivity Measured by Scanning Electrochemical Microscopy on Nickel-Based Alloy 600. *Electrochimica Acta* **2019**, *313*, 292–302.
- (42) Singh, K. K. Strain Hardening Behaviour of 316L Austenitic Stainless Steel. *Materials science and technology* **2004**, *20* (9), 1134–1142.
- (43) Chang, L.; Volpe, L.; Wang, Y. L.; Burke, M. G.; Maurotto, A.; Tice, D.; Lozano-Perez, S.; Scenini, F. Effect of Machining on Stress Corrosion Crack Initiation in Warm-Forged Type 304L Stainless Steel in High Temperature Water. *Acta Materialia* **2019**, *165*, 203–214.
- (44) Deng, P.; Peng, Q.; Han, E.-H.; Ke, W. Effect of the Amount of Cold Work on Corrosion of Type 304 Nuclear Grade Stainless Steel in High-Temperature Water. *Corrosion* **2017**, *73* (10), 1237–1249.